Journal of Fluorescence
https://doi.org/10.1007/s10895-024-03786-7

RESEARCH

Synthesis, Crystal Structure, Fluorescence and Theoretical Calculations of Three Zn(II)/Cd(II) Complexes with Bis-dentate N,N-Quinoline Schiff Base

Zhiyu Jia[1] · Jiahui Cao[1] · Wei Chen[2] · Zhou Yu[1] · Yangyang Song[1] · Yuwei Dong[1]

Received: 3 April 2024 / Accepted: 6 June 2024

Abstract

Three d^{10} metal complexes, **ZnL(OAc)$_2$** (**1**), **CdL(OAc)$_2$** (**2**) and **[CdL$_2$(NO$_3$)$_2$]·CH$_3$CN** (**3**) were synthesized using the ligand (*E*)-*N*-(3-methoxy-4-methylphenyl)-1-(quinolin-2-yl)methanimine (**L**) and characterized by FT-IR spectra, NMR spectra, and CHN elemental analysis. Single-crystal X-ray diffraction analysis revealed that complexes **1** and **2** are isostructural, with the central metal adopting a hexacoordinate octahedral geometry, while complex **3** adopts a triangular dodecahedron geometry. Thermal gravimetric analysis showed that these complexes exhibit good thermal stability. Solid-state fluorescence spectroscopy measurements demonstrated that complexes **1**–**3** exhibit bright yellow-green fluorescence (λ_{em} = 564 nm for **1**; 524 nm for **2**; 542 nm for **3**), suggesting their potential as photoluminescent materials. Furthermore, DFT calculations, including frontier molecular orbitals, energy levels, and surface electrostatic potential, provided insights into the structural and electronic spectral properties of complexes **1**–**3**.

Keywords d^{10} Metal Complexes · Schiff base · Fluorescence · Theoretical Calculations

Introduction

Schiff base ligands are obtained by condensation of the aldehydes and amines, which are widely used to prepare non-transition metal complexes and transition metal complexes [1–5]. Due to the advantages of Schiff base ligands, such as simple synthesis, good stability, and complexation ability, organic ligands ranging from rigid to flexible can be constructed by changing the structure of aldehydes and amines. They serve as molecular building blocks (similar to porphyrins) and coordinate with metals to synthesize new materials with outstanding potential [6, 7]. Among them, zinc/cadmium Schiff base complexes have been widely studied, mainly because they can be assembled into supramolecular functional materials with catalytic [8], biological imaging [9], thin film [10] and photophysical properties [11]. Metal complexes, resulting from the coordination of metal ions, balancing anions, and organic ligands, exhibit advantages such as tunable excitation and emission properties, straightforward synthesis methodologies, and a wide range of structural designs. These attributes offer the potential to produce intriguing supramolecular architectures and luminescent characteristics.

It is well-known that quinoline derivatives can construct luminescent metal–organic materials with various metal ions due to their large conjugated system and good coordination ability [12–14]. Keasberry et al. presented a study on the synthesis of the [Zn(**NNS**)$_2$] complex, employing the ligand quinoline-2-formaldehyde-4-methyl-3-thiosemicarbazone (**HNNS**), and single-crystal X-ray diffraction analysis showed that the central metal zinc exhibited a distorted octahedral configuration. The antibacterial activity of [Zn(**NNS**)$_2$] was evaluated, and the results indicated that it possessed stronger antibacterial activity compared to the **HNNS** ligand [15]. Salah et al. synthesized two novel zinc and cadmium complexes using quinoline derivatives, which

✉ Yangyang Song
songyyabc@nankai.edu.cn

✉ Yuwei Dong
dong_yuwei@163.com

[1] Institute of Catalysis for Energy and Environment, College of Chemistry & Chemical Engineering, Shenyang Normal University, Shenyang, Liaoning 110034, P. R. China

[2] School of Biotechnology and Health Sciences, Wuyi University, Jiangmen, Guangdong 529020, P. R. China

Published online: 03 July 2024

exhibited solvatochromic behavior with a red shift in $\pi \rightarrow \pi^*$ transition as the solvent polarity increased [16]. Demissie and colleagues synthesized a zinc(II) complex using the ligand 2-(2-hydroxyethyl)aminoquinoline-3-carboxaldehyde ($\mathbf{H_2L}$) as the starting material in a methanol solution with a metal-to-ligand ratio of 1: 2. Compared to the ligand, the metal complex exhibited intense fluorescence intensity and a blue shift in emission [17]. The fluorescence properties of these d^{10} metal complexes are extremely important due to their versatile applications in chemical sensors, photochemistry, and electroluminescent displays [18, 19].

Based on the above discussion, in our study, a Schiff base ligand (*E*)-*N*-(3-methoxy-4-methylphenyl)-1-(quinolin-2-yl) methanimine (**L**) with N2 coordination sites was synthesized using quinoline-2-carboxaldehyde and 3-methoxy-4-methylaniline, and the corresponding metal complexes **1**–**3** were synthesized under reflux conditions. The structures and photophysical properties of complexes **1**–**3**, as well as the relationship between their structure and fluorescence properties, were discussed in detail. The bright fluorescence emission of complexes **1**–**3** suggests potential applications in photoluminescent materials.

Experimental

Materials and Measurements

All the solvents and reagents (analytical grade) were used as received. All the materials for synthesis were purchased from Haohong Scientific Co., Ltd. (Shanghai, China). Elemental analyses of C, H and N were conducted using a Vario EL elemental analyzer. ^{1}H and ^{13}C NMR spectra of **L** and complexes **1**–**3** were obtained using a Bruker Avance–400 MHz spectrometer in DMSO-d_6 at 298 K. FT–IR spectra were recorded using a TENSOR II (Bruker) spectrophotometer using a KBr pellet in the range of 4000–400 cm^{-1}. Thermal gravimetry analysis (TGA) experiments were conducted with Versa Therm TGA instrument with a heating rate of 10 °C min^{-1} from 40 to 800 °C under a nitrogen atmosphere. Sample preparations for the TGA were carried out under air. UV – vis spectra were recorded by using a Shimadzu UH5300 (Japan) spectrophotometer in the range of 200–800 nm at room temperature. Fluorescence spectra were obtained using a Hitachi F-7100 FL spectrophotometer equipped with a 150 W xenon lamp as the excitation and emission source at room temperature, and the slit width of the acetonitrile solution fluorescence spectra was 5.0 nm both the excitation and emission, and that for the solid-state fluorescence spectra was 5.0 nm for excitation and 1.0 nm for emission. The sample concentration for UV – vis and fluorescence spectra testing was 2×10^{-5} mol L^{-1} in CH_3CN.

Synthesis of Complexes 1–3

The Schiff base (*E*)-*N*-(3-methoxy-4-methylphenyl)-1-(quinolin-2-yl)methanimine (**L**) was synthesized following a previously reported method [20]. Complexes **1**–**3** were synthesized along the reaction route depicted in Scheme 1. A mixture of the ligand **L** (0.0536 g, 0.2 mmol) and the corresponding metal salts of either $(Zn(OAc)_2 \cdot 2H_2O$ (0.0456 g, 0.2 mmol), $Cd(OAc)_2 \cdot 2H_2O$ (0.0535 g, 0.2 mmol) or $Cd(NO_3)_2 \cdot 4H_2O$ (0.0312 g, 0.1 mmol)) in 25 mL CH_3CN was refluxed at 80 ℃ for 4–5 h. After several days, yellow crystals of complexes **1**–**3** were collected by slow evaporation.

(*E*)-*N*-(3-methoxy-4-methylphenyl)-1-(quinolin-2-yl)methanimine (L) Yield: 84.60%, Color: Yellow. Anal. calc. for $C_{18}H_{16}N_2O$: C, 78.24; H, 5.84; N, 10.14. Found: C, 78.29; H, 6.03; N, 10.01. ^{1}H NMR (400 MHz, DMSO-d_6, δ): 8.86 (s, 1H, C*H*=N), 8.50 (d, *J*=8.8 Hz, 1H, Quinoline–H_3), 8.32 (d, *J*=8.4 Hz, 1H, Quinoline–H_6), 8.16 (d, *J*=8.4 Hz, 1H, Quinoline–H_2), 8.07 (d, *J*=8.0 Hz, 1H, Quinoline–H_9), 7.86 (t, *J*=7.2 Hz, 1H, Quinoline–H_8), 7.70 (t, *J*=7.6 Hz, 1H, Quinoline–H_7), 7.22 (d, *J*=7.6 Hz, 1H, Phene–H_5), 7.06 (s, 1H, Phene–H_2), 6.95 (d, *J*=8.0 Hz, Phene–H_6), 3.90 (s, 3H, –OCH_3), 2.20 (s, 3H, –CH_3) ppm. ^{13}C NMR (100 MHz, DMSO-d_6, δ): 160.21, 158.38, 155.04, 149.76, 147.90, 137.34, 131.19, 130.62, 129.65, 128.89, 128.53, 128.27, 125.29, 118.57, 113.85, 104.10, 55.81, 16.25 ppm. UV–vis (λ_{max}, CH_3CN): 252, 298, 348 nm.

$ZnL(OAc)_2$ (1) Yield: 81.50%, Color: Orange. Anal. calc. for $C_{22}H_{22}N_2O_5Zn$: C, 57.47; H, 4.82; N, 6.09. Found: C, 57.55; H, 4.73; N, 6.16. ^{1}H NMR (400 MHz, DMSO-d_6, δ): 8.87 (s, 1H, C*H*=N), 8.54 (d, *J*=6.8 Hz, 1H), 8.28 (d, *J*=8.8 Hz, 1H), 8.17 (d, *J*=7.2 Hz, 1H), 8.08 (d, *J*=8.0 Hz, 1H), 7.85 (t, *J*=7.2 Hz, 1H), 7.70 (t, *J*=7.6 Hz, 1H), 7.22 (d, *J*=7.6 Hz, 1H), 7.08 (s, 1H), 6.98 (d, *J*=6.8 Hz, 1H), 3.86 (s, 3H, –OCH_3), 2.16 (s, 3H, –CH_3), 1.79 (s, 6H, –OOCCH_3) ppm. ^{13}C NMR (100 MHz, DMSO-d_6, δ): 177.34, 167.76, 160.10, 158.48, 149.29, 131.24, 130.98, 130.96, 129.56, 129.12, 128.63, 125.61, 114.10, 104.31, 55.88, 22.87, 16.32 ppm. UV–vis (λ_{max}, CH_3CN): 244, 290, 354 nm.

$CdL(OAc)_2$ (2) Yield: 85.12%, Color: Lemon-yellow. Anal. calc. for $C_{22}H_{22}N_2O_5Cd$: C, 52.14; H, 4.38; N, 5.53. Found: C, 52.20; H, 4.40; N, 5.49. ^{1}H NMR (400 MHz, DMSO-d_6): 8.93 (s, 1H, C*H*=N), 8.59 (d, *J*=7.2 Hz, 1H), 8.27 (d, *J*=8.4 Hz, 2H), 8.10 (d, *J*=8.4 Hz, 1H), 7.87 (t, *J*=7.2 Hz, 1H), 7.72 (t, *J*=7.2 Hz, 1H), 7.23 (d, *J*=7.6 Hz, 1H), 7.15 (s, 1H), 7.04 (d, *J*=6.4 Hz, 1H), 3.86 (s, 3H, –OCH_3), 2.17 (s, 3H, –CH_3), 1.81 (s, 6H, –OOCCH_3) ppm. ^{13}C NMR (100 MHz, DMSO-d_6, δ): 178.45, 165.67, 160.16, 158.37, 148.39, 143.55, 131.23, 131.08, 130.85, 129.62, 128.63, 126.50, 114.16, 110.43, 106.11, 101.92, 55.90, 22.18, 16.33 ppm. UV–vis (λ_{max}, CH_3CN): 252, 300, 354 nm.

Scheme 1 Synthetic routes for complexes **1**–**3**

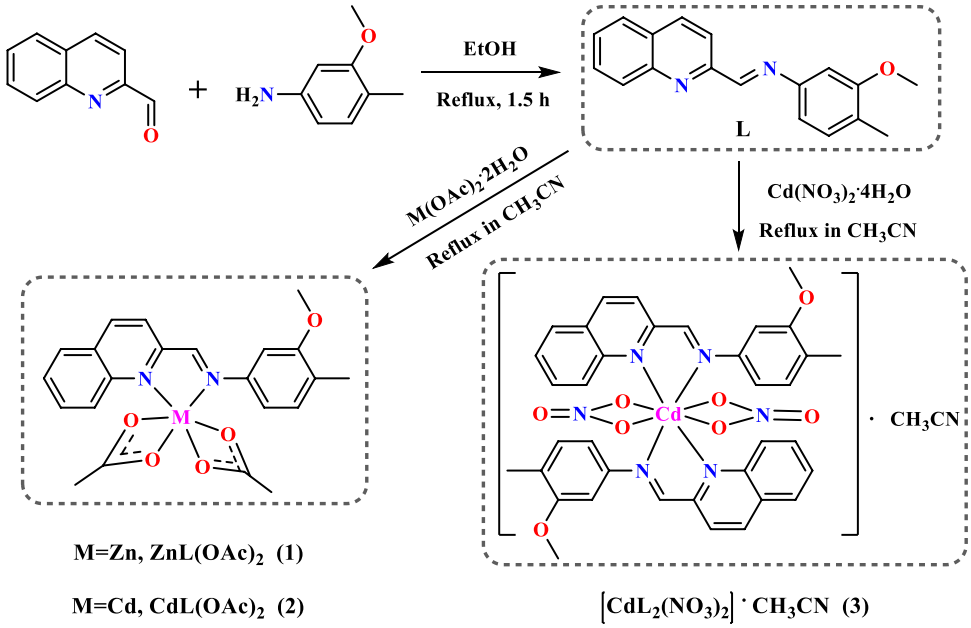

[$CdL_2(NO_3)_2$]·CH_3CN (3) Yield: 50.33%, Color: Orange. Anal. calc. for $C_{38}H_{35}N_7O_8Cd$: C, 54.98; H, 4.25; N, 11.81. Found: C, 54.83; H, 4.28; N, 11.75. ^{1}H NMR (400 MHz, DMSO-d_6): 8.82 (s, 1H, C*H*=N), 8.50 (d, *J*=8.8 Hz, 1H), 8.28 (d, *J*=8.8 Hz, 1H), 8.11 (d, *J*=7.6 Hz, 1H), 8.06 (d, *J*=8.4 Hz, 1H), 7.83 (t, *J*=7.6 Hz, 1H), 7.68 (t, *J*=7.2 Hz, 1H), 7.20 (d, *J*=7.6 Hz, 1H), 7.02 (s, 1H), 6.94 (d, *J*=7.6 Hz, 1H), 3.84 (s, 3H, –OCH_3), 2.15 (s, 3H, –CH_3), 2.05 (s, 1.5H, CH_3CN) ppm. ^{13}C NMR (100 MHz, DMSO-d_6, δ): 160.34, 160.08, 158.38, 156.89, 152.35, 147.84, 147.79, 131.24, 130.82, 129.61, 128.63, 128.45, 118.56, 113.98, 110.75, 104.14, 55.87, 16.31, 11.24 ppm. UV–vis (λ_{max}, CH_3CN): 248, 230, 374 nm.

Molecular Structure Determination

Crystallographic data were collected on a Rigaku R–AXIS RAPID IP diffractometer with graphite-monochromatized Cu·Kα radiation (λ = 1.54178 Å) at 298 K for complexes **1**–**3**. The structures were solved by the direct methods and refined with full-matrix least-squares on F^2 [21]. All non-hydrogen atoms were refined anisotropically, and hydrogen atoms were added theoretically. The structural information and results were stored in the Cambridge Crystallographic Data Centre (numbers: 2307441 for **1**; 2,330,760 for **2**; 2,307,440 for **3**).

Computational Details

Gaussian 09 program [22] was employed for DFT calculations. Density functional theory (DFT) calculations were performed using Beck's three-parameter hybrid exchange functional [23] and Lee, Yang and Parr correlation functional [24] B3LYP/6–31G (d). The calculated electronic density plots were prepared using the Gaussview 5.0.8. The Multiwfn [25] and VMD [26] software were used for more detailed analysis.

Results and Discussion

Description of Crystal Structures

The relevant crystallographic parameters for complexes **1**–**3** is summarized in Table 1. The complexes **$ZnL(OAc)_2$** (**1**) and **$CdL(OAc)_2$** (**2**) are crystallized in $P2_1/n$ space group of monoclinic system and $P\bar{1}$ space group of triclinic system, respectively. According to X-ray crystallography analysis, the structures of complexes **1** and **2** are isomorphic, as shown in Fig. 1. The central metal is hexacoordinate, coordinated with quinoline nitrogen (N1), imine nitrogen (N2) and four oxygen atoms (O2, O3, O4, O5) from acetate anions. In the crystal structure of **1**, the geometry around the Zn(II) ion is that of an octahedron, the equatorial plane of which is best described by the plane (N1/N2/Zn/O3/O5) and apical sites are taken by two oxygens (O2, O4) of two acetate anions (Fig. S1). In the crystal structure of **2**, the octahedral configuration around the Cd(II) ion features an equatorial plane occupied by one nitrogen (N2) and three oxygens (O2, O3 and O5), with the apical positions taken up by one nitrogen (N1) and one oxygen (O4). In both molecular structures, the maximum axial angles of complexes **1** (∠O2–Zn1–O4) and **2** (∠N1–Cd1–O4) are 150.97(15)° and 136.27(10)°,

Table 1 Crystal data and structure refinement for complexes **1**–**3**

Identification code	1	2	3
Empirical formula	$C_{22}H_{22}N_2O_5Zn$	$C_{22}H_{22}N_2O_5Cd$	$C_{38}H_{35}N_7O_8Cd$
Formula weight	459.78	506.81	830.13
Temperature/K	293(2)	293(2)	293(2)
Crystal system	Monoclinic	Triclinic	Triclinic
Space group	$P2_1/n$	$P\bar{1}$	$P\bar{1}$
a/Å	8.0208(2)	7.8323(3)	8.43270(10)
b/Å	20.2646(4)	11.4855(4)	12.7759(2)
c/Å	12.7898(3)	12.2964(5)	17.9385(3)
α/°	90	81.462(3)	82.7550(10)
β/°	93.323(2)	76.277(3)	81.4230(10)
γ/°	90	79.081(3)	76.8510(10)
Volume/Å^3	2075.34(8)	1048.89(7)	1852.35(5)
Z	4	2	2
ρ_{calc}/g·cm^{-3}	1.472	1.605	1.488
μ/mm^{-1}	1.956	1.077	5.245
F(000)	952	512	848
Crystal size/mm^3	0.34 × 0.32 × 0.3	0.34 × 0.32 × 0.3	0.34 × 0.32 × 0.3
Radiation	CuKα (λ = 1.54178)	MoKα (λ = 0.71073)	CuKα (λ = 1.54178)
Θ range for data collection/°	4.092 – 68.340	3.431 – 29.250	2.502 – 68.207
Index ranges	$-9 \le h \le 9$, $-24 \le k \le 20$, $-12 \le l \le 15$	$-10 \le h \le 10$, $-15 \le k \le 13$, $-16 \le l \le 16$	$-10 \le h \le 8$, $-15 \le k \le 15$, $-21 \le l \le 20$
Reflections collected/unique	10,791/3614	9063/4781	18,533/6544
Data/restraints/parameters	3614/0/311	4781/0/275	6544/0/492
Goodness-of-fit on F^2	1.089	1.042	1.037
Final R indexes [I > 2σ(I)][a]	$R_1 = 0.0590$, $wR_2 = 0.1474$	$R_1 = 0.0410$, $wR_2 = 0.0829$	$R_1 = 0.0642$, $wR_2 = 0.1613$
Final R indexes [all data][a]	$R_1 = 0.0626$, $wR_2 = 0.1515$	$R_1 = 0.0518$, $wR_2 = 0.0875$	$R_1 = 0.0659$, $wR_2 = 0.1636$
Largest diff. peak/hole /e·Å^{-3}	0.355/–1.094	1.783/–0.454	1.329/–3.146
CCDC number	2,307,441	2,330,760	2,307,440

[a] $R_1 = \sum||F_o| - |F_c||/\sum|F_o|$; $wR_2 = [\sum[w\,(F_o^2 - F_c^2)^2]/\sum[\,w\,(F_o^2)^2]]^{1/2}$

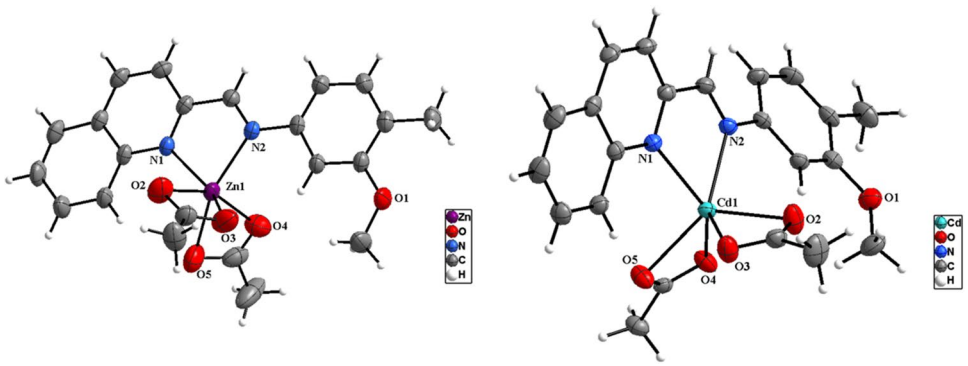

Fig. 1 ORTEP view of the molecular structures of complexes **1** (left) and **2** (right) with ellipsoid probability level 30%. Only metal atoms and heteroatom is labeled

respectively, indicating that the central metal atom is situated in a distorted octahedral environment. Tables S1–S4 present the important bond distances and angles parameters for the two complexes **1** and **2**. Notably, the N2–C10 bond distances are 1.264(3) Å for complex **1** and 1.267(4) Å for complex **2**, which are consistent with the imine bond in the literature structural data [27, 28]. The M–N bond lengths have significantly differ in the two complexes due to the difference in the radii of zinc and cadmium. Obviously, the bond distances of Zn1–N1 and Zn1–N2 in complex **1** are 2.104(2) Å and 2.142(2) Å, respectively, which are shorter than those of in complex 2, with Cd1–N1 of 2.326(3) Å and

Cd1–N2 of 2.351(3) Å. As shown in Fig. S2, the dihedral angles between the quinoline ring (C1-C9/N1) and benzene ring (C11-C16) are 5.494° and 33.981° in complexes **1** and **2**, respectively, indicating that the two rings in complex **1** are almost coplanar. Molecules with good coplanarity often possess specific chemical properties and reactivity [29–31].

In the crystals of these two complexes, the intermolecular hydrogen bonding interactions (listed in Table 2) further connect the mononuclear molecules to generate a supramolecular architecture. In the supermolecular assembly of **1**, no classic hydrogen bonds were found and only weak interactions exhibited intermolecular C–H···O bonds interactions, which played vital role in stabilizing the crystal structure [32, 33]. As shown in Fig. 2, molecules of complex **1** were linked by two hydrogen bonds C3–H3···O4 and C10–H10···O2 to form the different dimers. These dimers were further linked by C7–H7···O3 hydrogen bonding to give rise to 3-D supramolecular structure in space. The molecular packing in the crystals of complex **2** was very distinct from that of complex **1**. Two C–H···O hydrogen bonds C10–H10···O3 and C22–H22C···O4 linked adjacent molecules to form a one-dimensional T-shaped chain arrangement along *c*-axis (Fig. 2).

X-ray crystallography analysis has revealed that complex $\mathbf{[CdL_2(NO_3)_2]\cdot CH_3CN}$ (**3**) forms a 2:1 ligand to metal stoichiometry, and crystallizes in the triclinic system with $P\bar{1}$ space group and consists of one Cd(II) ion, two ligand **L**, and two nitrate anions participating in coordination (Fig. 3). In addition, the asymmetric unit of complex **3** contains a crystalline acetonitrile molecule. Some important bond distances and angles of complex **3** are listed in Tables S5 and S6. Each cadmium ion was associated with two quinoline nitrogen atoms (N1, N3), two imine nitrogen atoms (N2, N4) in the ligand, and four

Table 2 Hydrogen bond lengths (Å) and angles (◦) for complexes **1–3**

Complex	D–H···O	*d*(D–H)/ Å	*d*(H···A)/ Å	*d*(D···A)/ Å	∠(DHA)/ (◦)
1	C3–H3···O4	0.930	2.581	3.343	139.411(1)
	C7–H7···O3	0.930	2.583	3.289	133.116(1)
	C10–H10···O2	0.930	2.500	3.326	148.167(1)
2	C10–H10···O2	0.930	2.533	3.386	152.754(5)
	C22–H22C···O4	0.960	2.512	3.459	168.569(4)
3	C16–H16···O4	0.930	2.542	3.362	147.238(2)
	C30–H30···O3	0.930	2.484	3.381	161.832(2)

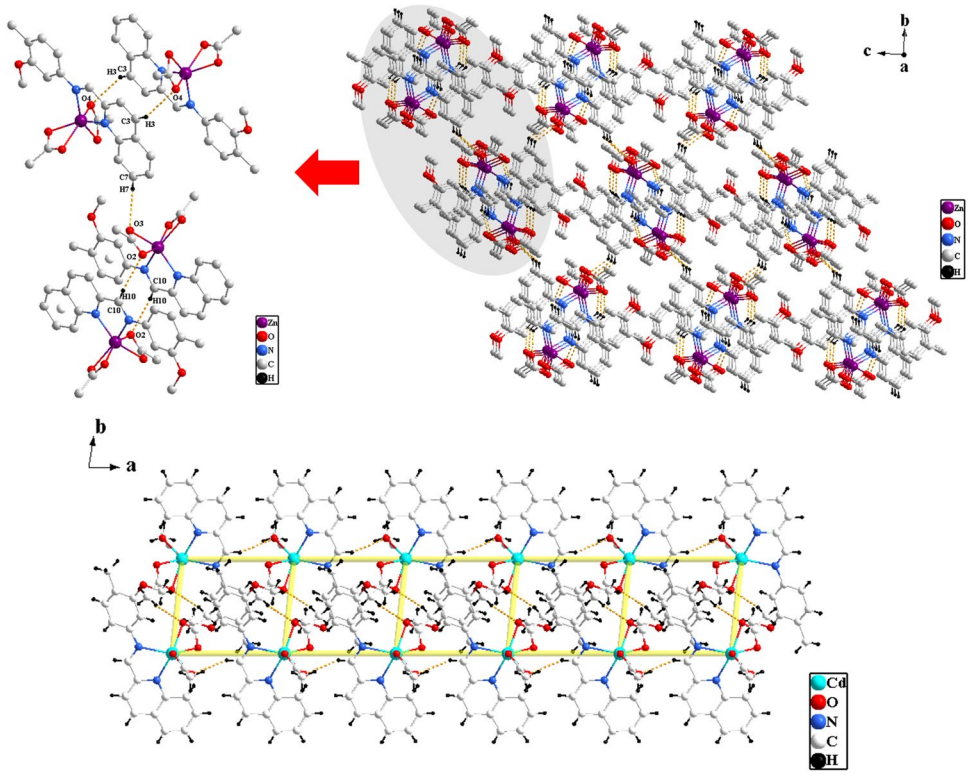

Fig. 2 Intermolecular hydrogen bonds with selective atom numbering scheme, view of 3-D supramolecular assembly of **1** (up) and 1-D chain of **2** along *ab*-plane (down)

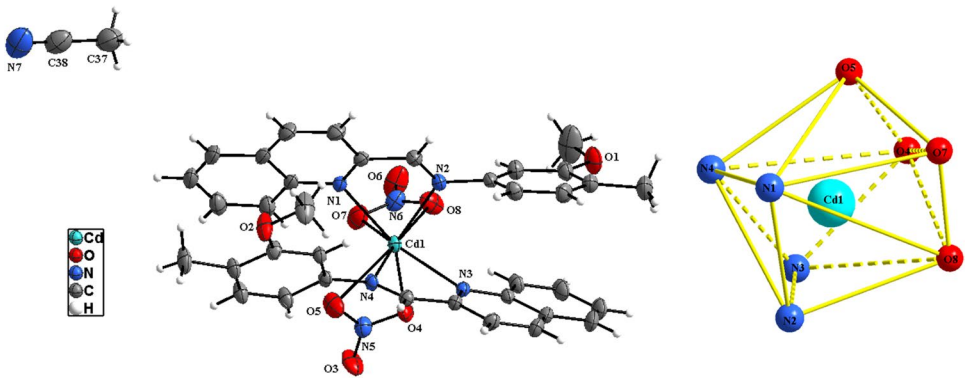

Fig. 3 ORTEP view of the molecular structure of complex **3** (left) with ellipsoid probability level 30%. Only metal atoms and heteroatom is labeled. The coordination geometry of complex **3** (right)

oxygen atoms (O4, O5, O7, O8) from the nitrate ions. The central metal cadmium(II) ion of complex **3** can be best described as a triangular dodecahedron (Fig. 3). Due to the participation of two ligand **L** molecules in coordination, the structure of complex **3** is relatively distorted, with the dihedral angles between the quinoline ring and the benzene ring being 49.507° (Fig. S3) and 51.396° (Fig. S4), respectively.

In the supermolecular assembly of **3**, two C–H···O hydrogen bonds C16–H16···O4 and C30–H30···O3 linked adjacent molecules to form a one-dimensional chain arrangement along *b*-axis (Fig. 4). In addition, one-dimensional chains were further linked into a two-dimensional layered structure through π–π stacking. For the π–π stacking interaction, the centroid–centroid distance of the two rings (N3/C19-C27) and the two rings (N1/C1-C9) were 3.744 Å and 3.725 Å, respectively. These rings were stacked with a dihedral angle close to 0 ◦.

TGA, FT-IR and NMR Analysis

The thermal stabilities of complexes **1**–**3** were examined under an N_2 atmosphere from 40 to 800 °C, as depicted in Fig. 5. This investigation aimed to verify the crystalline solvent content and assess the structural stability of these complexes. For complex **1**, its TGA curve showed weight loss only when the temperature reached 217 °C, and the product above 600 °C might be ZnO (found: 17.41%; calcd: 17.38%). Similarly, complex **2** began to undergo structural collapse and ligand decomposition at temperatures above 188 °C, and the product above 600 °C should be CdO (found: 25.72%; calcd: 25.63%). For complex **3**, the crystallized solvent molecule acetonitrile was released in the temperature range of 78 to 153 °C (found: 4.90%; calcd: 4.95%), and a second weight loss occurred above 238 °C along with structural collapse and ligand decomposition. The final product above 600 °C may be CdO (found: 15.62%; calcd: 15.65%). From

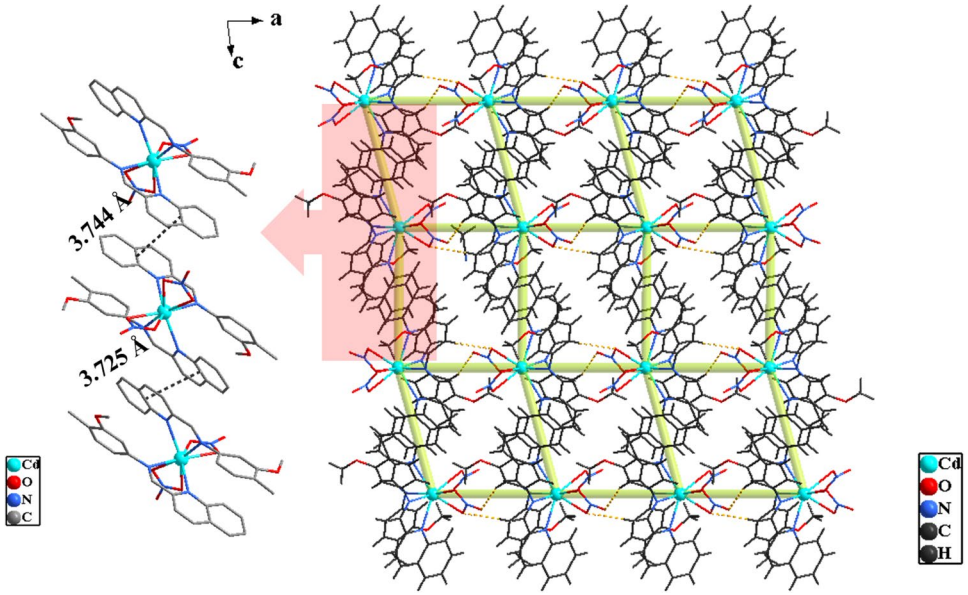

Fig. 4 Packing diagram of **3** along *b*-axis through intermolecular hydrogen bonds and π–π interactions. Acetonitrile molecules are omitted for clarity

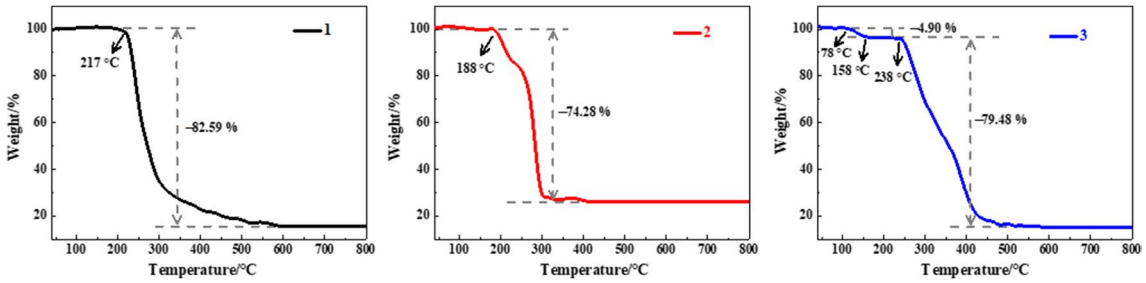

Fig. 5 The TGA curves for complexes **1**–**3**

the results of the analysis, complex **3** containing crystalline solvent (238 °C) exhibited higher thermal stability compared to complexes **1** (217 °C) and **2** (188 °C).

The FT-IR spectra of the free ligand **L** and complexes **1**–**3** (Figs. S5–S8) provide the significant information about the binding of ligand **L** to the metal atom. Table 3 presents the stretching frequencies for υ(Ar–H), υ(–CH_3), υ(C=N), υ(C–O), and δ(–CH_3) modes of ligand **L** with corresponding shifts. In this paper, the Schiff base ligand **L** can form coordination bonds with Zn(II)/Cd(II) ions via the quinoline nitrogen and imine groups. In complexes **1**–**3**, the stretching bands in the 3046–3079 cm^{-1} region are assigned to the (C–H) of aromatic ring, bands at 1609–1618 cm^{-1} signify the (C=N) of imine group, 1228–1234 cm^{-1} represent the (C–O) corresponding to the methoxy group [34, 35]. Moreover, the stretching vibration and the deformation vibration peaks of –CH_3 were found in the FT-IR spectra of complexes **1**–**3**. Due to the formation of complexes, the IR bands of complexes **1**–**3** were slightly shifted compared with those of ligand **L**. Notably, at 1628 cm^{-1}, the ligand **L** has a a characteristic C=N stretching band, which is shifted to lower frequencies by 10–19 cm^{-1} in complexes **1**–**3**, implying the coordination of the imine nitrogen and Zn(II)/Cd(II) ions [36, 37]. In addition, the new non-ligand stretching bands in the low-frequency regions 519–522 cm^{-1} are attributed to υ(M–N) [38, 39], which can also be evidence for the formation of M–N coordination bond.

The ^{1}H NMR spectra of the non-magnetic zinc/cadmium complexes provide further evidence for the ligand **L** bonding mode (Figs. S9–S12). The ^{1}H NMR spectra of **L** and **1**–**3** were recorded in DMSO–d_6 at room temperature. Compared with the ^{1}H NMR data of ligand **L** (δ 8.86 ppm), the proton signals of the imine (–CH=N) group appear as singlets at δ 8.87, 8.93, and 8.82 ppm for complexes **1**–**3**, respectively. The chemical shifts of imine proton hydrogen are slightly changed due to the coordination of imine nitrogen with Zn(II)/Cd(II). The proton hydrogens located on the quinoline ring and benzene ring of complexes **1**–**3** exhibit a precise one-to-one correspondence with their respective chemical structures. Detailed data of NMR spectra, including the chemical shifts, peak patterns, coupling constants of different hydrogen/carbon are listed in Section 2.2. In addition, the proton signals of the methoxy (–OCH_3) group appear as singlets at δ 3.86, 3.86, and 3.84 ppm, protons of the methyl (–CH_3) group attached to the phene ring as singlet at δ 2.16, 2.17, and 2.15 ppm in complexes **1**–**3**, respectively. In contrast to the ligand **L**, the presence of the protons of the acetate (–$OOCCH_3$) group signals was observed in complexes **1** and **2**, located at 1.79 and 1.81 ppm, respectively. Additionally, the proton peaks of crystallized acetonitrile molecules (δ 2.05 ppm) appeared in complex **3**, which is consistent with the structure analyzed by single-crystal X-ray diffraction. The integration values of different proton are consistent with the number of proton atoms in the structure of complexes **1**–**3**, and no organic impurities were observed [40, 41].

In the ^{13}C NMR spectra of the ligand **L** and complexes **1**–**3** (Figs. S13–S16), the peaks were consistent in accordance with the total number of carbon atoms in the structure. The peaks corresponds to characteristic imine (–CH=N) carbons, which appeared at 160.21, 177.34, 178.45, 160.34 ppm in **L** and **1**–**3**, respectively. Peaks are observed in the ranges of 55.81–55.90 ppm and 16.25–22.87 ppm, corresponding to –OCH_3 carbon and –CH_3 carbon in the structure respectively. To sum up, ^{1}H and ^{13}C chemical shifts in the NMR spectra of complexes **1**–**3** display the expected shifts of those resonances due to proton and carbon atoms close to N donor atoms involved in bonding to zinc/cadmium.

Table 3 Important IR data (cm^{-1}) of **L** and its complexes **1**–**3**

Compound	υ(Ar–H)	υ(–CH_3)	υ(C=N)	υ(C–O)	δ(–CH_3)	υ(M–N)
L[a]	3056	2972, 2829	1628	1237	1451, 1371	–
$ZnL(OAc)_2$ (1)	3046	2945, 2838	1618	1232	1462, 1381	519
$CdL(OAc)_2$ (2)	3062	2965, 2838	1609	1228	1469, 1382	520
$[CdL_2(NO_3)_2]\cdot CH_3CN$ (3)	3079	2974, 2838	1616	1234	1459, 1382	522

[a] The IR data of ligand **L** were obtained from literature [20]

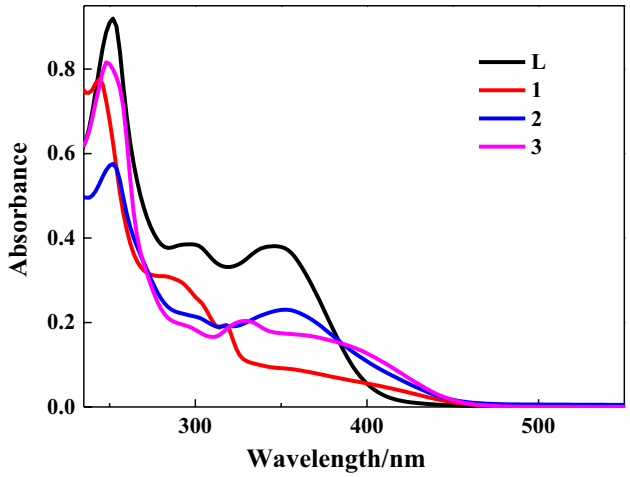

Fig. 6 UV–Vis spectra of ligand **L** and complexes **1**–**3** in acetonitrile solution

UV–Vis Spectroscopy

The electronic spectra of the ligand **L** and its complexes **1**–**3** (2×10^{-5} mol L^{-1}) were recorded in acetonitrile solution. As shown in Fig. 6, the absorption bands of complexes **1**–**3** are similar to those of **L**. The ligand **L** shows three peaks at 252, 298 (sh), and 348 nm. The high-energy bands at 252 and 298 (sh) nm belong to the $\pi\rightarrow\pi^*$ transition of the quinoline ring, and the low energy bands at 348 nm are mainly caused by $n\rightarrow\pi^*$ transitions of imine group (–CH = N) [42, 43]. the UV–Vis absorption data are summarized in Table 4. The extinction coefficients of these bands fall into the range 10^4–10^5 M^{-1} cm^{-1}. The red shift of peaks in complexes **1**–**3** is mainly due to ligand-based transitions, displaying that the quinoline nitrogen atom and imine nitrogen atom are coordinated with Zn(II)/Cd(II) ions [44, 45]. Due to the presence of d^{10} electron configuration in Zn(II)/Cd(II), no low-energy $d\rightarrow d$ transition was observed in **1**–**3** [46, 47].

Fluorescence Properties

As we mentioned before, the Zn(II)/Cd(II) complexes can serve as potential luminescent materials for organic light-emitting diode (OLED) applications [48]. Therefore, we investigated the solid-state luminescent properties of complexes **1**–**3** at room temperature. As shown in Fig. 7, the ligand **L** and complexes **1**–**3** exhibit similar fluorescence emission bands, with maximum emission peaks are located at 518, 564, 524, and 542 nm, respectively. These values exhibit a red shift relative to the position of the maximum emission peak in acetonitrile solution. The fluorescence data are summarized in Table 4. The photoluminescence properties of the Zn(II)/Cd(II) complexes are primarily attributed to intramolecular ligand emissions, which are due to the presence of the d^{10} electronic configuration [49, 50]. Compared to the free ligand **L**, the fluorescence emission peaks of complexes **1**–**3** exhibit a significant red shift and an increase in fluorescence intensity. This can be attributed to the enhanced structural rigidity of complex resulting from coordination [51]. In addition, the differences in fluorescence intensity among complexes **1**–**3** may be related to the heavy atom effect of cadmium [52]. Under the irradiation of a 365 nm UV lamp, the Zn(II) complex **1** exhibits bright orange-yellow fluorescence (Fig. 7), which may be related to the good coplanarity of its structure (the dihedral angle is 5.494°, close to 0°). The fluorescence of complexes **1**–**3** in acetonitrile solution is weak (Fig. 7), which may be due to solution quenching [53, 54]. These results show that complexes **1**–**3** can be used as a potential luminescent materials.

DFT Studies

We calculated the HOMO and LUMO of ligand **L** and complexes **1**–**3** using the B3LYP method with the 6–31G(d)/LANL2DZ basis set. The optimized geometries are derived from the single-crystal structures of complexes **1**–**3**. The electron clouds of the highest occupied molecular orbital (HOMO) of **L** and **1**–**3** are primarily distributed over the benzene rings and C = N double bonds, whereas the electron clouds of the lowest unoccupied molecular orbital (LUMO) are localized on the quinoline rings. Consequently, the transitions observed in complexes **1**–**3** can be ascribed to metal-perturbed ligand internal $\pi\rightarrow\pi^*$ transitions. As depicted in Fig. 8, the energy gaps between HOMO and LUMO of **L** and **1**–**3** are 3.53, 3.02 eV, 3.08 eV and 3.30 eV, respectively. A smaller energy gap implies a longer maximum absorption

Table 4 UV–Vis absorption and fluorescence emission data of **L** and its complexes **1**–**3**

Compound	Absorption/nm (ε/M^{-1} cm^{-1}, CH_3CN)		Assignements	Fluorescence/nm		Assignements
				Solid sate	CH_3CN	
L	252 (45,978), 298^{sh} (19,250)	348 (19,018)	$\pi\rightarrow\pi^*$, $n\rightarrow\pi^*$	518	412	$\pi\rightarrow\pi^*$, $\pi\rightarrow\pi^*$
$ZnL(OAc)_2$ (**1**)	244 (38,769), 290^{sh} (14,982)	354 (4528)	$\pi\rightarrow\pi^*$, $n\rightarrow\pi^*$	564	415	$\pi\rightarrow\pi^*$, $\pi\rightarrow\pi^*$
$CdL(OAc)_2$ (**2**)	252 (28,778), 300^{sh} (10,685)	354 (11,503)	$\pi\rightarrow\pi^*$, $n\rightarrow\pi^*$	524	460	$\pi\rightarrow\pi^*$, $\pi\rightarrow\pi^*$
$[CdL_2(NO_3)_2]\cdot CH_3CN$ (**3**)	248 (40,800), 330^{sh} (9131)	374 (8118)	$\pi\rightarrow\pi^*$, $n\rightarrow\pi^*$	542	468	$\pi\rightarrow\pi^*$, $\pi\rightarrow\pi^*$

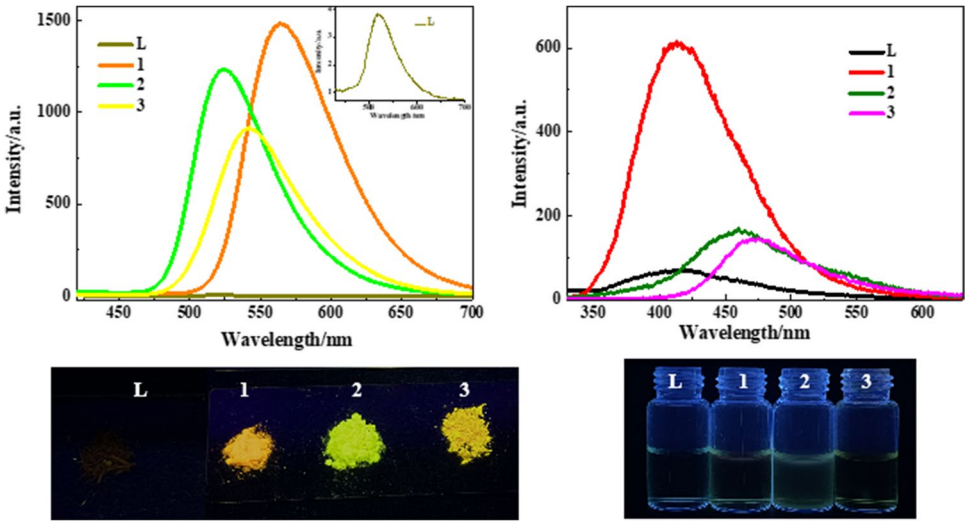

Fig. 7 Fluorescence emission spectra of the ligand **L** and complexes **1**–**3**. Left: in the solid-state (λ_{ex} = 365 nm, Ex slit: 5.0 nm, Em slit: 1.0 nm); right: in acetonitrile solution. The solid-state (left) and liquid-state (right) fluorescence photos under 365 nm UV lamp irradiation

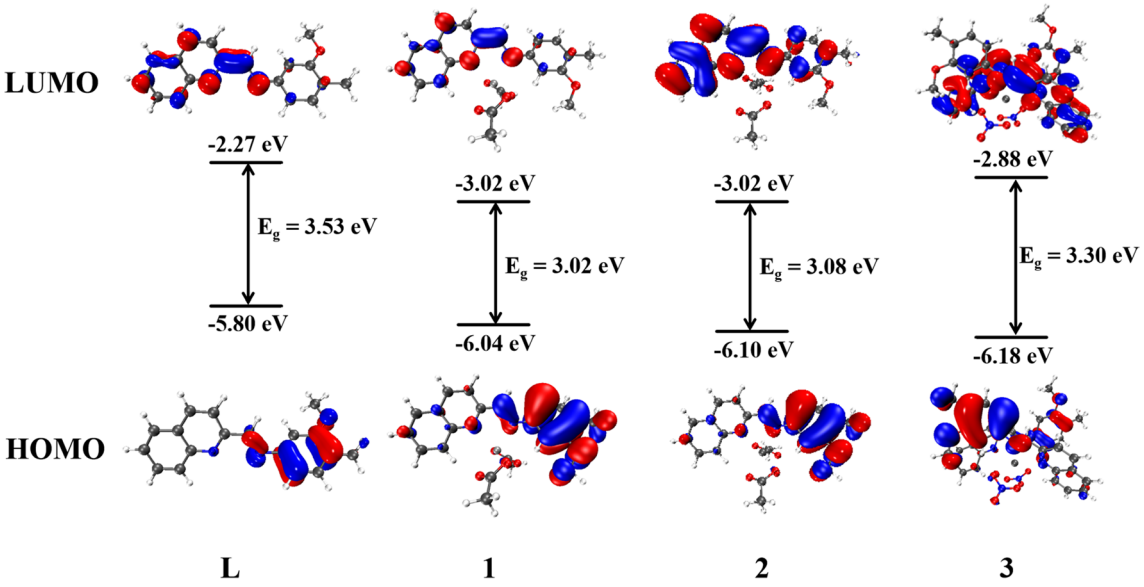

Fig. 8 Frontier molecular orbitals of the free ligand **L** and complexes **1**–**3** and their LUMO–HOMO gaps

wavelength [55], which is generally consistent with their experimental spectroscopic results.

ESP Analysis

The electrostatic surface potential (ESP) pertains to the distribution of electrostatic potential across a specific surface enveloping a molecule. It is intimately associated with the electronegativity, electron density, partial charges, dipole moment, and chemical reactivity inherent to the molecule [56, 57]. ESP stands as a pivotal instrument in the elucidation and anticipation of molecular reactions. Divergent colors are employed to visualize the magnitudes of electrostatic potential across distinct surface areas, thereby offering a precise representation of the electrostatic potential distribution on the molecular surface [58]. When the ESP exhibits blue on the molecular surface, it denotes the presence of a negative electrostatic potential, thereby implying a tendency towards the occurrence of electrophilic reactions [59]. As seen from Fig. 9 in ligand **L** and complexes **1**–**3**, the regions exhibiting negative potential are situated around the benzene rings and nitrogen atoms, suggesting that hydrogen bonds can readily form in this particular region [27].

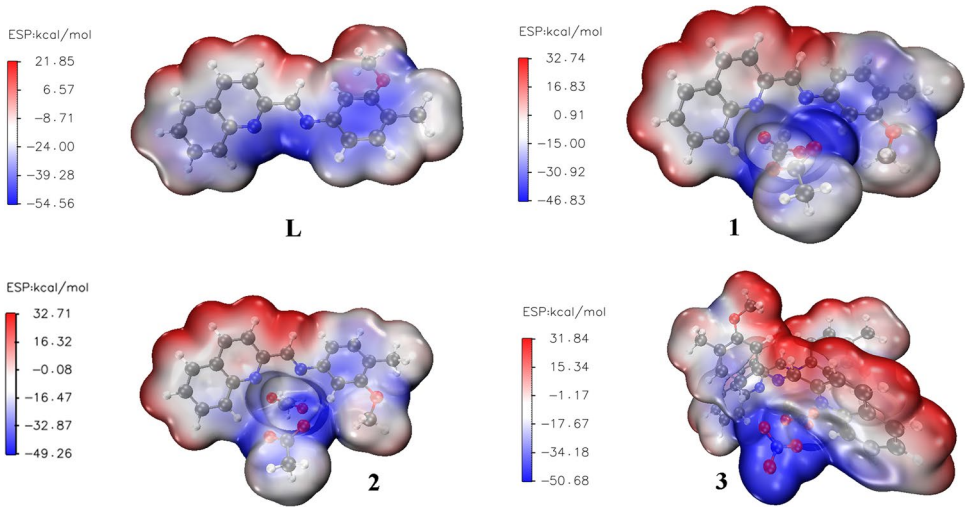

Fig. 9 Molecular electrostatic potential surface map of the ligand **L** and complexes **1**–**3** (red regions means electron-poor regions, blue regions refering to electron-rich regions)

Conclusions

In this study, we studied the synthesis, characterizations and crystal structures of three Zn(II) and Cd(II) complexes of a Schiff base, (*E*)-*N*-(3-methoxy-4-methylphenyl)-1-(quinolin-2-yl)methanimine. In complexes **1**–**3**, intermolecular C-H···O hydrogen bonds and π–π stacking interactions connect molecules to form different supermolecular structures, which further stabilize the crystal structures. Further, fluorescence analysis of complexes **1**–**3** showed that the coordination interaction between the metal and ligand enhances the fluorescence emission intensity and leads to a red shift in emission. The solid-state fluorescence emissions of **1**–**3** were observed at 564, 524, and 564 nm, respectively, exhibiting bright yellow-green fluorescence, suggesting their potential as luminescent materials. In addition, the mechanism of fluorescence enhancement in complexes was verified through theoretical calculations.

Supplementary Information The online version contains supplementary material available at https://doi.org/10.1007/s10895-024-03786-7.

Author Contributions Zhiyu Jia: writing–original draft, methodology, investigation, data curation. Jiahui Cao: methodology, investigation, data curation. Wei Chen: Crystal structure analysis. Zhou Yu: investigation, resources. Yangyang Song: DFT studies, resources. Yuwei Dong: writing–original draft, methodology, investigation.

Funding This work was supported by National Natural Science Foundation of China (22102107 and 22302131), the Young and Middle-aged Science and Technology Innovation Talents Program of Shenyang (RC220317).

Data Availability The data used to support the findings of this study are included within the article.

Declarations

Ethical Approval As this work does not deal with any human or animal object so no need of ethical approval is needed.

Competing Interests The authors declare no competing interests.

References

1. Whiteoak CJ, Salassaa G, Kleij AW (2012) Recent advances with π-conjugated salen systems. Chem Soc Rev 41:622–631. https://doi.org/10.1039/c1cs15170c
2. Li XJ, Xie SQ, Hu YZ, Xiang J, Wang LM, Li RL, Chen M, Wang FB, Liu Q, Chen XQ (2021) AIEgen modulated per-functionalized flower-like IRMOF-3 frameworks with tunable light emission and excellent sensing properties. Chem Commun 57:2392–2395. https://doi.org/10.1039/d0cc08403d
3. Laube C, Taut JA, Kretzschmar J, Zahn S, Knolle W, Ullman S, Kahnt A, Kersting B, Abel B (2020) Light controlled oxidation by supramolecular Zn(II) Schiff-base complexes. Inorg Chem Front 7:4333–4346. https://doi.org/10.1039/d0qi00980f
4. Li T, Wang YF, Yin Z, Li J, Peng X, Zeng MH (2022) The sequential structural transformation of a heptanuclear zinc cluster towards hierarchical porous carbon for supercapacitor applications. Chem Sci 13:10786–10791. https://doi.org/10.1039/d2sc03987g
5. Li L, Wang L, Peng X, Tao S, Zeng MH (2022) Nickel–salen as a model for bifunctional OER/UOR electrocatalysts: pyrolysis temperature–electrochemical activity interconnection. Inorg Chem Front 9:1973–1983. https://doi.org/10.1039/d2qi00226d
6. Mondal I, Basak T, Banerjee S, Chattopadhyay S (2020) A theoretical insight on the rigid hydrogenbonded network in the solid state structure of two zinc(II) complexes and their strong fluorescence behaviors. CrystEngComm 22:3005–3019. https://doi.org/10.1039/d0ce00125b
7. Nirumand L, Farhadi S (2021) Cobalt(II) Schiff base chemically grafted onto magnetic amino-functionalized reduced graphene oxide nanosheets for highly rapid and selective removal of methyl orange. New J Chem 45:11946–11959. https://doi.org/10.1039/d1nj02118d
8. Mazet C, Jacobsen EN (2008) Dinuclear (salen)Al complexes display expanded scope in the conjugate cyanation of α, β-unsaturated imides. Angew Chem Int Ed 47:1762–1765. https://doi.org/10.1002/chin.200827090
9. Chakraborty T, Mukherjee S, Parveen R, Chandra A, Samantac D, Das D (2021) A combined experimental and theoretical rationalization of an unusual zinc(II)-mediated conversion of

18-membered Schiff-base macrocycles to 18-membered imine–amine macrocycles with imidazolidine side rings: an investigation of their bio-relevant catalytic activities. New J Chem 45:2550–2562. https://doi.org/10.1039/d0nj05635a
10. Koo BH, Lim KS, Ryu DW, Lee WR, Kohb EK, Hong CS (2013) Synthesis, structures and magnetic characterizations of isostructural tetranuclear Ln_4 clusters (Ln = Dy, Ho, and Eu). Dalton Trans 42:7204–7209. https://doi.org/10.1039/c3dt00056g
11. Qiao D, Wang JY, Zhang LY, Dai FR, Chen ZN (2019) Aggregation-induced emission enhancement and reversible mechanochromic luminescence of quinoline-based zinc(II)–Schiff base complexes. Dalton Trans 48:11045–11051. https://doi.org/10.1039/c9dt02177a
12. Yuan GZ, Zhang Q, Wang ZP, Song K, Yuan XM, Wang YZ, Zhang LY (2017) Assembly of four 8-quinolinate-based multinuclear complexes: the effect of substituents on core structures and photoluminescent properties. Inorg Chem Fron 4:764–772. https://doi.org/10.1039/c7qi00082k
13. Bella SD (2021) Lewis acidic zinc(II) salen-type Schiff-base complexes: sensing properties and responsive nanostructures. Dalton Trans 50:6050–6063. https://doi.org/10.1039/d1dt00949d
14. Yan XJ, Song XX, Mu XY, Wang Y (2019) Mechanochromic luminescence based on a phthalonitrile-bridging salophen zinc(II) complex. New J Chem 43:15886–15891. https://doi.org/10.1039/c9nj03704g
15. Nurin Sakinatul Hayati Haji Damit, Malai Haniti Sheikh Abdul Hamid, Nur Sabrina Rahayu Haji Abdul Rahman, Siti Nor Hashimah Haji Ilias, Natasha Ann Keasberry (2021) Synthesis, structural characterisation and antibacterial activities of lead(II) and some transition metal complexes derived from quinoline-2-carboxaldehyde 4-methyl-3-thiosemicarbazone, Inorg Chim Acta 527:120557. https://doi.org/10.1016/j.ica.2021.120557
16. Ibrahim MA, Emara AAA, Taha A, Adly OMI, Nabeel AI, Aziz MA, Salah N (2023) Synthesis, characterization, TD-DFT, molecular docking, biological applications, and solvatochromic studies of some new metal complexes derived from semicarbazone of pyrano[3,2-*c*]quinoline-3-carboxaldehyde. Appl Organomet Chem 37:e7169. https://doi.org/10.1002/aoc.7169
17. Damena T, Alem MB, Zeleke D, Desalegn T, Eswaramoorthy R, Demissie TB (2022) Novel zinc(II) and copper(II) complexes of 2-((2-hydroxyethyl)amino)quinoline-3-carbaldehyde for antibacterial and antioxidant activities: a combined experimental, DFT, and docking studies. ACS Omega 30:26336–26352. https://doi.org/10.1021/acsomega.2c02205
18. Ilmi R, Kansız S, Al Rasbi NK, Husband J, Dege N, Khan MS (2023) Synthesis, X-ray crystal structure and determination of non-covalent interactions through Hirshfeld surface analysis of a pure red emitting asymmetrical octacoordinated Sm(III) complex. Polyhedron 246:116673. https://doi.org/10.1016/j.poly.2023.116673
19. Liu X, Hamon JR (2019) Recent developments in penta-, hexa- and heptadentate Schiff base ligands and their metal complexes. Coord Chem Rev 389:94–118. https://doi.org/10.1016/j.ccr.2019.03.010
20. Dong YW, Wang Y, Song Y, Yu Z, Yu Z, Zhao Z, Wang LY (2024) A simple and rapid quinoline Schiff base as a fluorescent probe for Zn^{2+} and its application in test strips. ChemistrySelect 9:e202400389. https://doi.org/10.1002/slct.202400389
21. Sheldrick GM (1999) SHELXTL NT Crystal Structure Analysis Package, Version 5.10, Bruker AXS, Analytical X-ray System, Madison, WI
22. Huang H, Wang YX, Wang B, Zhuang SQ, Pan B, Yang X, Wang L, Yan CL (2013) Controllably tunable phenanthroimidazole–carbazole hybrid bipolar host materials for efficient green electrophosphorescent devices. J Mater Chem C 1:5899–5908. https://doi.org/10.1039/c3tc30832d
23. Chen S, Wu YK, Zhao Y, Fang DN (2015) Deep blue organic light-emitting devices enabled by bipolar phenanthro[9,10-*d*]imidazole derivatives. RSC Adv 5:72009–72018. https://doi.org/10.1039/c5ra13814k
24. Yuan Y, Chen JX, Lu F, Tong QX, Yang QD, Mo HW, Ng TW, Wong FL, Guo ZQ, Ye J, Chen Z, Zhang XH, Lee CS (2013) Bipolar phenanthroimidazole derivatives containing bulky polyaromatic hydrocarbons for nondoped blue electroluminescence devices with high efficiency and low efficiency roll-off. Chem Mater 25:4957–4965. https://doi.org/10.1021/cm4030414
25. Lu T, Chen FW (2012) Multiwfn: a multifunctional wavefunction analyzer. J Comput Chem 33:580–592. https://doi.org/10.1002/jcc.22885
26. Humphrey W, Dalke A, Schulten K (1996) VMD: visual molecular dynamics. J Mol Graph 14:33–38. https://doi.org/10.1016/0263-7855(96)00018-5
27. Yan YB, Yang RW, Zhang HW, Zhang Y, Dong WK (2024) Crystal structure and luminescent mechanochromism of a quinoline-appended acylhydrazone ligand and its Zn(II) complex. J Mol Struct 1299:137148. https://doi.org/10.1016/j.molstruc.2023.137148
28. Chai LQ, An HL, Chen TT, Cai YY (2024) Structural, spectroscopic, theoretical calculation and Hirshfeld surface analyses of 3-D supramolecular dinuclear zinc(II) and copper(II) complexes. J Mol Struct 1299:137151. https://doi.org/10.1016/j.molstruc.2023.137151
29. Leong DW, Shao YW, Ni Z, Bhuvanesh N, Ozerov OV (2024) A bis(PCN) palladium pincer complex with a remarkably planar 2,5-diarylpyrazine core. Dalton Trans 53:6520–6523. https://doi.org/10.1039/d3dt04248k
30. Kumar D, Muniappan K, Chinnusamy S, Shanmugam E (2024) Substituent position dependent photophysical properties of indolebarbituric and thiobarbituric acid based molecular rotors. ChemistrySelect 9:e202301776. https://doi.org/10.1002/slct.202301776
31. Ji XZ, Cheng HW, Schuster NJ, LeCroy GS, Zhang S, Wu YL, Michalek L, Nguyen BNT, Chiong JA, Schrock M, Tomo Y, Rech J, Salleo A, Gam S, Lee GH, Tok JBH, Bao ZA (2023) Tuning the mobility of indacenodithiophene-based conjugated polymers via coplanar backbone engineering. Chem Mater 6:256–265. https://doi.org/10.1021/acs.chemmater.3c02006
32. Guerrero M, Pou R, Bay´es-García L, Font-Bardia M, Sort J, Pons J, Ayll´on JA (2018) Syntheses, supramolecular architectures and photoluminescence properties of Zn (II) complexes based on 3,5-dihydroxybenzoic and pyridine/pyrazole derived ligands. Inorg Chem Commun 96:34–38.https://doi.org/10.1016/j.inoche.2018.07.047
33. Xu ZX, Yu TZ, Zhao YL, Zhang H, Zhao GY, Li JF, Chai LQ (2016) A new starshaped carbazole derivative with polyhedral oligomeric silsesquioxane core: crystal structure and unique photoluminescence property. J Fluoresc 26:149–154. https://doi.org/10.1007/s10895-015-1694-y
34. Mukherjee D, Sarkar K, Reja S, Bakibillah M, Guha S, Mandal NK, Naskar JP, Das RK (2023) Mononuclear Zn(II) complex based on N_2O ligand compartment: first case to detect nitro explosives. J Fluoresc. https://doi.org/10.1007/s10895-023-03431-9
35. Li J, Ren HJ, Li JT (2023) Application values of two Cu(II) schiff base coordination complexes on blue fluorescent materials. J Fluoresc. https://doi.org/10.1007/s10895-023-03423-9
36. El-Shalakany H, Ramadan R, Sayed M (2024) New bivalent metal chelates based on an NO-donor Schiff base ligand: synthesis, structural characterization, DFT simulation, biological evaluation, and molecular docking analysis. Inorg Chem Commun 159:111826. https://doi.org/10.1016/j.inoche.2023.111826
37. Marchetti F, Pettinari R, Verdicchio F, Tombesi A, Scuri S, Xhafa S, Olivieri L, Pettinari C, Choquesillo-Lazarte D, García-García A, Rodríguez-Diéguez A, Galindo A (2022) Role of hydrazone

substituents in determining the nuclearity and antibacterial activity of Zn(II) complexes with pyrazolone-based hydrazones. Dalton Trans 51:14165–14181. https://doi.org/10.1039/d2dt02430f
38. Paul S, Barman P (2024) Exploring diaminomaleonitrile-derived Schiff base ligand and its complexes: synthesis, characterization, computational insights, biological assessment, and molecular docking. J Mol Struct 1296:136941. https://doi.org/10.1016/j.molstruc.2023.136941
39. Elantabli F, Mohamed R, El-Medani S, Haukka M, Ramadan R, Afifi M (2024) Structural investigations of new tridentate-phenylacetohydrazide Schiff base metal chelates: X-ray diffraction, Hirshfeld surface analyses, DFT, antibacterial and molecular docking studies. J Mol Struct 1299:137230. https://doi.org/10.1016/j.molstruc.2023.137230
40. Bal M, Köse A (2024) Schiff bases containing 1,2,3-triazole group and phenanthroline: synthesis, characterization, and investigation of DNA binding properties. J Photochem Photobiol A Chem 448:115320. https://doi.org/10.1016/j.jphotochem.2023.115320
41. Kose A, Erkan S, Tümer M (2023) A series of phenanthroline-imine compounds: Computational, OLED properties and fluorimetric sensing of nitroaromatic compounds. Spectrochim, Acta Part A Mol Biomol Spectrosc 286:122006. https://doi.org/10.1016/j.saa.2022.122006
42. Divyashree NR, Hosakere DR, Yathirajan HS, Bhavya NR, Mahendra M, Muzaffar I, Chandan S, Raghavendra G, Shiva P (2023) Highly selective and sensitive fluorescent "TURN-ON" furan-based Schiff base for zinc(II) ion probing: chemical synthesis, DFT studies, and X-ray crystal structure. New J Chem 44:17420–17433. https://doi.org/10.1039/d3nj02466k
43. Naskar B, Dhara A, Maiti D, Kukułka M, Mitoraj M, Srebro-Hooper M, Prodhan C, Chaudhuri K, Goswami S (2019) Aggregation induced emission based sensing platform for selective detection of Zn^{2+}: experimental and theoretical investigations. ChemPhysChem 20:1630–1639. https://doi.org/10.1002/cphc.201900113
44. Himadri PG, Anmol S, Pranjit B, Diganta C (2022) A new potential ONO Schiff-Base ligand and its Cu(II), Zn(II) and Cd(II) Complexes: synthesis, structural elucidation, theoretical and bioactivity studies. Inorg Chem Commun 146:110153. https://doi.org/10.1016/j.inoche.2022.110153
45. Kargar H, Fallah-Mehrjardi M, Behjatmanesh-Ardakani R, Munawar KS, Ashfaq M, Tahir MN (2022) Diverse coordination of isoniazid hydrazone Schiff base ligand towards iron(III): synthesis, characterization, SC-XRD, HSA, QTAIM, MEP, NCI, NBO and DFT study. J Mol Struct 1250:131691. https://doi.org/10.1016/j.molstruc.2021.131691
46. Damena T, Alem MB, Zeleke D, Desalegn T, Eswaramoorthy R, Demissie TB (2022) Synthesis, characterization, and biological activities of zinc(II), copper(II) and nickel(II) complexes of an aminoquinoline derivative. Front Chem 10:1–21. https://doi.org/10.3389/fchem.2022.1053532
47. Majumdara D, Dasc D, Sreejithd S, Nage S, Deyb S, Mondalb S, Bankuraa K, Mishra D (2019) Synthesis, characterizations and single crystal structure of di-nuclear azidobridged Cd(II) coordination polymer with Schiff base precursor ($H_2L_{pent}^{OMe}$): DFT, fluorescence, solvatochromism and in vitro antimicrobial assay. Inorg Chim Acta 496:119069. https://doi.org/10.1016/j.ica.2019.119069
48. Barwiolek M, Jankowska D, Chorobinski M, Kaczmarek-Kędziera A, Łakomska I, Wojtulewskic S, Muzioła T (2021) New dinuclear zinc(II) complexes with Schiff bases obtained from *o*-phenylenediamine and their application as fluorescent materials in spin coating deposition. RSC Adv 11:24515–24525. https://doi.org/10.1039/d1ra03096e
49. Ullmann S, Schnorr R, Laube C, Abel B, Kersting B (2018) Photoluminescence properties of tetrahedral zinc(II) complexes supported by calix[4]arene-based salicylaldiminato ligands. Dalton Trans 47:5801–5811. https://doi.org/10.1039/c8dt00757h
50. Wong CC, Tsai MJ, Wu JY (2022) Zinc– and copper–salicyaldimine complexes: Simultaneous observation of both metal–ligand coordination and weak CH···N contact about a single N-donor and the transmetallation reactions. J Solid State Chem 316:123622. https://doi.org/10.1016/j.jssc.2022.123622
51. Tsai MJ, Wong CC, Wu JY (2023) Structures, photophysical properties, and optical sensing of zinc– and copper–salicyaldimine complexes. J Photochem Photobiol A Chem 443:114808. https://doi.org/10.1016/j.jphotochem.2023.114808
52. Williams NJ, Gan W, Reibenspies JH, Hancock RD, Steric P (2009) Control of the relative strength of chelation enhanced fluorescence for zinc(II) compared to cadmium(II): metal ion complexing properties of tris(2-quinolylmethyl)amine, a crystallographic, UV-visible, and fluorometric study. Inorg Chem 48:1407–1415. https://doi.org/10.1021/ic801403s
53. Lin JY, Liu B, Yu MN, Lin ZQ, Zhang XW, Sun C, Cabanillas-Gonzalez J, Xie LH, Liu F, Ou CJ, Bai LB, Han YM, Xu M, Zhu WS, Trevor AS, Paul NS, Donal DCB (2019) Ultrastable supramolecular self-encapsulated wide-bandgap conjugated polymers for large-area and flexible electroluminescent devices. Adv Mater 31:1804811. https://doi.org/10.1002/adma.201804811
54. Solanki JD, Siddiqui I, Gautam P, Gupta VK, Jou JH, Surati KR (2022) Blue fluorescent Zinc (II) complexes bearing schiff base ligand for solution-processed organic light-emitting diodes with CIEy≤ 0.09. Opt Mater 134:113222. https://doi.org/10.1016/j.optmat.2022.113222
55. Zhang SN, Huang MM, Lu H, Ma ZY, Wang ZJ, Yang JP (2022) Three-arm star-shaped aniline derivatives: Tunable photoluminescence, aggregation-induced emission and reversible acid-base vapor fluorescence response. J Photochem Photobiol A 432:114098. https://doi.org/10.1016/j.jphotochem.2022.114098
56. Enbaraj E, Jeyashri KR, Logeshwari G, Manikandan H, Sivakumar K (2023) Synthesis, crystal structure, Hirshfeld surface analysis and theoretical studies of bis(substituted benzylidene) ethan-1,2-diamines. J Mol Struct 1275:134605. https://doi.org/10.1016/j.molstruc.2022.134605
57. Elangovan N, Alomar SY, Sowrirajan S, Rajeswari B, Nawaz A, Kalanthoden AN (2023) Photoluminescence property and solvation studies on (E)-N-(pyrimidin-2yl)-4-((3,4,5-trimethoxy benzylidede) amino) benzene sulfonamide; synthesis, structural, topological analysis, antimicrobial activity and molecular docking studies. Inorg Chem Commun 155:111019. https://doi.org/10.1016/j.inoche.2023.111019
58. Vennila M, Rathikha R, Muthu S, Jeelani A, Irfan A (2022) Theoretical structural analysis (FT-IR, FT-R), solvent effect on electronic parameters NLO, FMO, NBO, MEP, UV (IEFPCM model), Fukui function evaluation with pharmacological analysis on methyl nicotinate. Comput Theor Chem 1217:113890. https://doi.org/10.1016/j.comptc.2022.113890
59. Zhan HB, Zhang HW, Jiang JJ, Wang Y, Fei X, Tian J (2022) Influence of intramolecular hydrogen bond formation sites on fluorescence mechanism. Chin Phys B 31:038201. https://doi.org/10.1088/1674-1056/ac29ad